University of Kentucky
UKnowledge

Mechanical Engineering Faculty Publications

Mechanical Engineering

1-2015

Numerical Investigation on Charring Ablator Geometric Effects: Study of Stardust Sample Return Capsule Heat Shield

Haoyue Weng
University of Kentucky, kimomt@gmail.com

Alexandre Martin
University of Kentucky, alexandre.martin@uky.edu

Right click to open a feedback form in a new tab to let us know how this document benefits you.

Follow this and additional works at: https://uknowledge.uky.edu/me_facpub

Part of the Aerodynamics and Fluid Mechanics Commons, Computer Sciences Commons, and the Space Vehicles Commons

Repository Citation

Numerical Investigation on Charring Ablator Geometric Effects: Study of Stardust Sample Return Capsule Heat Shield

AIAA-2015-0211

AIAA SciTech, 5-9 January 2015, Kissimmee, FL

Numerical Investigation on Charring Ablator Geometric Effects: Study of Stardust Sample Return Capsule Heat Shield

Haoyue Weng[*] and Alexandre Martin[†]

University of Kentucky, Lexington, KY, 40506

Sample geometry is very influential in small charring ablative articles where 1D assumption might not be accurate. In heat shield design, 1D is often assumed since the nose radius is much larger than the thickness of charring. Whether the 1D assumption is valid for the heat shield is unknown. Therefore, the geometric effects of Stardust sample return capsule heat shield are numerically studied using a material response program. The developed computer program models material charring, conductive heat transfer, surface energy balance, pyrolysis gas transport and orthotropic material properties in 3D Cartesian coordinates. Simulation results show that the centerline temperatures predicted by 3D model are quite close to 1D model at the surface, but not the case inside the material. The pyrolysis surface gas blowing behaviors are quite similar but differences are observed at later time. Orthotropic model predicted a very different heat shield response to both the isotropic model and the 1D model.

I.   Introduction

Hypersonic planetary entry vehicles, such as Mars Science Laboratory (MSL) vehicle[1] and Stardust sample return capsule (SRC),[2] use charring ablative materials as Thermal Protection Systems (TPS), due to their effectiveness and light-weight. Charring ablative materials are made of non-pyrolyzing fibrous matrices (carbon, ceramic, etc.) impregnated with pyrolyzing resin materials (phenolic, silicon, etc.). One of the features of charring ablative materials is to absorb the aerodynamic heat, through endothermic reactions of pyrolysis and ablation.[3] Pyrolysis is the process in which the pyrolyzing resin gradually carbonizes at high temperature, losing mass and generating pyrolysis gas. Governed by inner pressure gradients, the generated pyrolysis gas travels within the porous material and blows through the ablator surface. The other phenomenon ablation, occurs in a thin layer near the surface, and refers to the mass removal of the char (composed of non-pyrolyzed and residual carbonized material) through oxidation, sublimation, and spallation.

Numerous material response programs that modeled ablation and pyrolysis were developed in 1D,[4,5,6,7,8,9] since 1D is computational cheap. The 1D assumption is based on the fact that the heat shield of a planetary entry vehicle usually has a much larger nose radius than the thickness of charring, and the stagnation surface can be considered to be flat. With the increment of computational capabilities, several multidimensional material response solvers were developed,[10,11,12,13,14] and multidimensional effects were studied. Recently, the authors investigated the effects of pyrolysis gas transport within test articles in arc-jet facilities.[10] Using the material response module of KATS (Kentucky Aerodynamic and Thermoresponse System), they found the 1D assumption might not be valid for small samples, especially due to the inner gas transport and the strong blowing through the side walls. It is as well important to investigate whether the 1D assumption is valid for an entire heat shield. However, few literatures have looked into the 3D behavior of an actual heat shield with consideration of pyrolysis gas transport, to either support or question the 1D assumption.

---

*Graduate Research Assistant, Department of Mechanical Engineering, Student Member AIAA

†Assistant Professor, Department of Mechanical Engineering, Associate Faculty Center for Computational Science, AIAA Senior Member

American Institute of Aeronautics and Astronautics Paper AIAA-2015-0211

Stardust mission returned extraterrestrial samples gathered from a comet tail, by sending a sample return capsule (SRC) back to Earth on 2006.[2] Since then (as well as before the mission), many researchers have studied/predicted the aerodynamics of the SRC geometry, providing surface heat flux and pressure distributions along the reentry trajectory.[15, 16, 2, 17] As a result, the Stardust SRC is a perfect candidate to investigate the performance of an entire heat shield in 3D. Using these surface distributions as boundary conditions, the whole heat shield is simulated in 3D, and the results are compared with the 1D model, attempting to justify or question the 1D assumption, as well as to find any phenomena that were overlooked due to the lack of dimension.

II.   Stardust Sample Return Capsule

Figure 1 and 2 shows the geometric information and a post flight photo of the Stardust SRC, respectively. The heat shield geometry has a round nose, the radius of which is 0.2202 m. The thickness of the heat shield
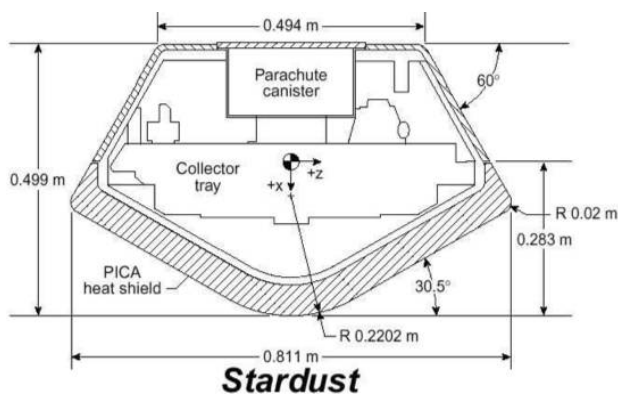

Figure 1: Stardust SRC geometry[16]

Figure 2: Post flight photo of Stardust SRC[18]

is 6.45 cm and the total measured recession is 0.65 cm.[2]

II.A.   Heat Shield Material

The forebody heat shield of the SRC was manufactured as a single piece, the material of which was made of phenolic impregnated carbon ablator (PICA);[19] the after body is covered with silicone elastomeric charring ablator (SLA-561V).[20] In this study, the heat shield material selected in the simulation is TACOT (Theoretical Ablative Composite for Open Testing).[21] TACOT is a fictitious material that based on PICA, and it has very similar performance compared to PICA. The original TACOT assumes isotropic material, with single permeability value for virgin and char state of the ablator. However, charring ablative materials often exhibit transverse isotropic transport behaviors, due to the fiber orientation.[22] In particular, two orientations are identified: in-plane (IP) and through-the-thickness (TTT) directions. In this work, a transverse isotropic Klinkenburg permeability model is implemented, based on an experimental measurement of PICA:[23]

$$K_{IP} = K_{0,IP}(1 + b_{IP}/p), \tag{1}$$
$$K_{TTT} = K_{0,TTT}(1 + b_{TTT}/p). \tag{2}$$

The effective permeability is then presented by a three-by-three matrix:

$$\boldsymbol{K} = \begin{pmatrix} K_{xx} & K_{xy} & K_{xz} \\ K_{yx} & K_{yy} & K_{yz} \\ K_{zx} & K_{zy} & K_{zz} \end{pmatrix} = \boldsymbol{R} \begin{pmatrix} K_{IP} & & \\ & K_{IP} & \\ & & K_{TTT} \end{pmatrix}, \tag{3}$$

where $\boldsymbol{R}$ is a rotation matrix depending on the rotation angles. Assuming the rotation angles (counterclockwise using right hand rule) are α, θ, and γ for rotation axes x, y, and z, respectively, the rotation matrices

American Institute of Aeronautics and Astronautics Paper AIAA-2015-0211

are:

$$\boldsymbol{R}_x(\alpha) = \begin{pmatrix} 1 & 0 & 0 \\ 0 & \cos\alpha & -\sin\alpha \\ 0 & \sin\alpha & \cos\alpha \end{pmatrix}, \tag{4}$$

$$\boldsymbol{R}_y(\theta) = \begin{pmatrix} \cos\theta & 0 & \sin\theta \\ 0 & 1 & 0 \\ -\sin\theta & 0 & \cos\theta \end{pmatrix}, \tag{5}$$

$$\boldsymbol{R}_z(\gamma) = \begin{pmatrix} \cos\gamma & -\sin\gamma & 0 \\ \sin\gamma & \cos\gamma & 0 \\ 0 & 0 & 1 \end{pmatrix}. \tag{6}$$

Then the overall rotation matrix is obtained by the product of all of the individual rotation matrices:

$$\boldsymbol{R} = \boldsymbol{R}_z(\gamma)\boldsymbol{R}_y(\theta)\boldsymbol{R}_x(\alpha). \tag{7}$$

Note that the order of matrices in the multiplication is determined by the inverse order of rotation in the geometry of concern. In this study, for example, the computational mesh for the Stardust heat shield is a 2 degree slice rotated around z-axis, so the cell center orthotropic directions within the material are obtained by rotation around y-axis by an angle θ ($0 \leq \theta \leq 30.5\,°$) first and rotation around z-axis by an angle $\gamma = 1\,°$; no rotation around x-axis is required. The overall rotation matrix is thus calculated by:

$$\boldsymbol{R} = \boldsymbol{R}_z(\gamma)\boldsymbol{R}_y(\theta) = \begin{pmatrix} \cos\gamma & -\sin\gamma & 0 \\ \sin\gamma & \cos\gamma & 0 \\ 0 & 0 & 1 \end{pmatrix} \begin{pmatrix} \cos\theta & 0 & \sin\theta \\ 0 & 1 & 0 \\ -\sin\theta & 0 & \cos\theta \end{pmatrix}. \tag{8}$$

Similarly, the transverse isotropic thermal conductivity is given as:

$$\boldsymbol{k}_s = \begin{pmatrix} k_{xx} & k_{xy} & k_{xz} \\ k_{yx} & k_{yy} & k_{yz} \\ k_{zx} & k_{zy} & k_{zz} \end{pmatrix} = \boldsymbol{R} \begin{pmatrix} k_{IP} & & \\ & k_{IP} & \\ & & k_{TTT} \end{pmatrix}. \tag{9}$$

The carbon fiber orientation of the Stardust SRC ablator was aligned with the vehicle surface, providing minimum TTT thermal conductivity.[24] Since the geometry of the SRC heat shield is not a flat surface, paralleled fiber orientations require location dependent TTT angles. Figure 3 illustrates the TTT angles at different locations of the ablator. For the geometry of Stardust heat shield, the TTT angle in the front nose region can be calculated using inverse trigonometric functions:

$$\theta_1 = \arctan\left(\frac{x}{z + 0.2202}\right), \tag{10}$$

and the TTT angle for the rest of the heat shield material is constantly $\theta_2 = 30.5°$.

III. Equations and Models

The governing equations of the material response module in KATS include a pyrolysis gas mass conservation, a time accurate gas momentum transport model, a multi-component solid decomposition model, and a mixture energy conservation (with a surface energy balance). These equations are solved in a stationary Cartesian coordinate system, using a finite volume method. The governing equations can be summarized in a general form:

$$\frac{\partial\mathbf{Q}}{\partial\mathbf{P}}\frac{\partial\mathbf{P}}{\partial t} + \nabla\cdot(\mathbf{F} - \mathbf{F_d}) = \mathbf{S}. \tag{11}$$

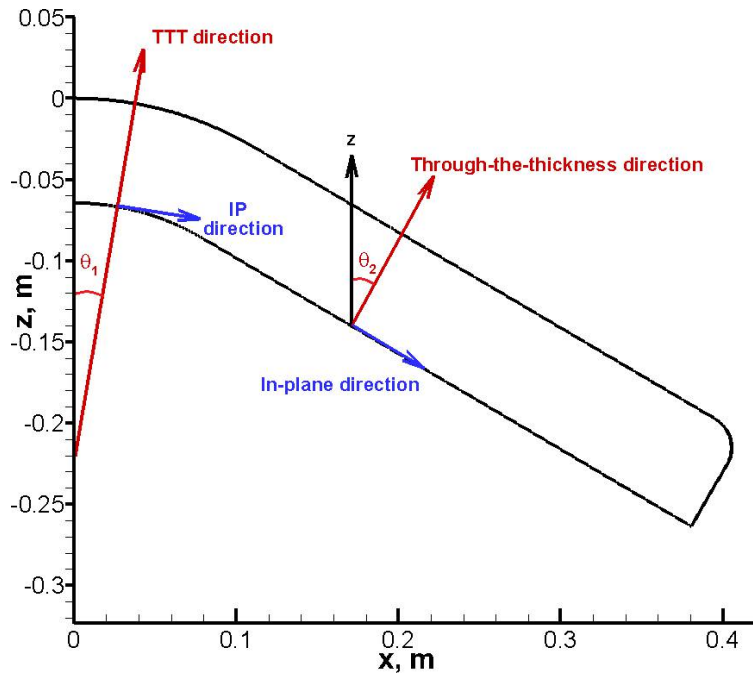American Institute of Aeronautics and Astronautics Paper AIAA-2015-0211

Figure 3: Illustrations of different fiber orientations within the material

Each component (bold font) in Eq. (11) represents a vector or a matrix:

$$
\mathbf{Q} = \begin{pmatrix} \phi\rho_{g_1} \\ \vdots \\ \phi\rho_{g_{ngs}} \\ \rho_{s_1} \\ \vdots \\ \rho_{s_{nss}} \\ \phi\rho_g u \\ \phi\rho_g v \\ \phi\rho_g w \\ \phi E_g + E_s \end{pmatrix}, \qquad
\mathbf{P} = \begin{pmatrix} p_1 \\ \vdots \\ p_{ngs} \\ \rho_{s_1} \\ \vdots \\ \rho_{s_{nss}} \\ u \\ v \\ w \\ T \end{pmatrix}, \qquad
\mathbf{S} = \begin{pmatrix} \omega_{g_1} \\ \vdots \\ \omega_{g_{ngs}} \\ \omega_{s_1} \\ \vdots \\ \omega_{s_{nss}} \\ D_x \\ D_y \\ D_z \\ S_D \end{pmatrix}, \tag{12}
$$

$$
\mathbf{F} = \begin{pmatrix} \phi\rho_{g_1} u & \phi\rho_{g_1} v & \phi\rho_{g_1} w \\ & \vdots & \\ \phi\rho_{g_{ngs}} u & \phi\rho_{g_{ngs}} v & \phi\rho_{g_{ngs}} w \\ 0 & 0 & 0 \\ & \vdots & \\ 0 & 0 & 0 \\ \phi\rho_g u^2 + p & \phi\rho_g vu & \phi\rho_g wu \\ \phi\rho_g uv & \phi\rho_g v^2 + p & \phi\rho_g wv \\ \phi\rho_g uw & \phi\rho_g vw & \phi\rho_g w^2 + p \\ \phi\rho_g uH & \phi\rho_g vH & \phi\rho_g wH \end{pmatrix}, \qquad
\mathbf{F}_d = \begin{pmatrix} & & \\ & & \\ & \mathbf{0} & \\ & & \\ & & \\ F_{cond,x} & F_{cond,y} & F_{cond,z} \end{pmatrix}, \tag{13}
$$

where ngs is number of gas species, nss is number of solid species, ϕ is porosity, ωs are reaction rates of the species, Ds are source terms that accounts for diffusive effects in the momentum equations, S_D is a diffusive

American Institute of Aeronautics and Astronautics Paper AIAA-2015-0211

source in the energy equation, and $\boldsymbol{F}_{cond} = (F_{cond,x}, F_{cond,y}, F_{cond,z})$ are conductive heat flux components in the three Cartesian axes.

III.A.   Solid decomposition model

The solid material in KATS is modeled with nss components. Each component has a volume fraction Γ_i. The overall solid density is computed by the sum of volume fraction times component density:

$$\rho_{s_t} = \sum_{i=1}^{nss} \Gamma_i \rho_{s_i}. \tag{14}$$

The decomposition rate of each solid component is modeled in a modified Arrhenius fashion:

$$\frac{\partial \rho_{s_i}}{\partial t} = \omega_{s_i} = -\rho_{s_{i,v}} \left(\frac{\rho_{s_i} - \rho_{s_{i,c}}}{\rho_{s_{i,v}}} \right)^{\psi_i} A_i e^{-E_i/(RT)}, \quad T > T_{reac,i}. \tag{15}$$

Aside from the Arrhenius equation $A_i e^{-E_i/(RT)}$, the term $\rho_{s_{i,v}} \left(\frac{\rho_{s_i} - \rho_{s_{i,c}}}{\rho_{s_{i,v}}} \right)^{\psi_i}$ provides extra control to the reaction rate. Note that, $\rho_{s_{i,v}}$ and $\rho_{s_{i,c}}$ are respectively virgin and char density of the solid component i. When a solid component is fully depleted, $\rho_{s_i} = \rho_{s_{i,c}}$, Eq. (15) becomes zero and no more decomposition occurs.

A phenomenological three-components (or two-stage) model is often applied for resin decomposition in charring ablators.[4] This is also the default model for TACOT. In this case, three virtual solid components are modeled and $nss = 3$. The volume fractions Γ_i, are taken to be 1/2.

III.B.   Pyrolysis gas model

The pyrolysis gas species are assumed to be in chemical equilibrium, that an overall gas mass conservation is solved and $ngs = 1$. The gas properties (*e.g.* molar mass, heat capacity) are obtained via equilibrium data.

The pyrolysis gas generation rate balances with the sum of decomposition rates of solid components:

$$\omega_g = -\sum_{i=1}^{nss} \Gamma_i \omega_{s_i}. \tag{16}$$

III.C.   Pyrolysis gas transport model

Typically, pyrolysis gas transport inside charring ablators is modeled with 1D Darcy's law.[25,7,5] In many 2D or 3D solvers, the gas transport was not modeled.[11,12] In KATS, the gas transport is modeled with a set of momentum conservations given in Eq. (11), (12) and (13). The momentum equations are essentially Euler equations derived in porous control volume. The source terms Ds account for diffusive effects due to the porous material, and are based on models. For instance, if Darcy's correlation is desired, Ds are obtained by solving the following system via Gauss elimination method:

$$\boldsymbol{K}\boldsymbol{D} = -\phi\mu\boldsymbol{V}, \tag{17}$$

where $\boldsymbol{K}$ is an anisotropic permeability matrix given in section II.A.

III.D.   Mixture energy model

KATS assumes thermal equilibrium for the pyrolysis gas and the solid components, based on a study by Gosse.[26] As shown in Eq. (11), only one mixture energy equation is considered and $T = T_g = T_s$.

The conductive heat flux, or the $\boldsymbol{F}_{cond}$ in $\mathbf{F}_d$ in Eq. (13), is also given in an anisotropic fashion:

$$\boldsymbol{F}_{cond} = \boldsymbol{k}_s \begin{pmatrix} \partial T/\partial x \\ \partial T/\partial y \\ \partial T/\partial z \end{pmatrix}. \tag{18}$$

Note that for isotropic material, Eq. (18) yields: $\boldsymbol{F}_{cond} = k\nabla T$.

The energy source S_D, is given as the following so as to be in consistent with the Ds in the momentum equations:

$$S_D = \begin{pmatrix} D_x \\ D_y \\ D_z \end{pmatrix} \begin{pmatrix} u & v & w \end{pmatrix} = D_x u + D_y v + D_z w. \tag{19}$$

III.E.   Surface energy balance

An energy balance equation is solved at the exposing surface to calculate the penetrated heat flux that conducted to the material:

$$\dot{q}''_{pen} = (\rho_e u_e C_{h_0}) \left(\frac{C_h}{C_{h_0}} \right) (h_r - h_w) + \dot{q}''_{rad} - \epsilon \sigma (T_w^4 - T_\infty^4) - \dot{m}''_g h_w. \tag{20}$$

Note that, surface recession is not modeled in KATS, therefore, the surface energy balance does not include the energy absorbed by the ablation, and the resultant temperature are expected to be higher than the ones modeled with ablation. On the right hand side of Eq. (20), $(\rho_e u_e C_{h_0})$ is the uncorrected convective heat transfer coefficient, (C_h/C_{h_0}) is the correction factor, h_r is the recovery enthalpy, $\dot{q}''_{rad}$ is the absorbed radiation heat flux, $\epsilon \sigma (T_w^4 - T_\infty^4)$ is the re-radiation to the environment, and $\dot{m}''_g h_g$ is the energy loss due to the pyrolysis gas blowing.

The correction to the heat transfer coefficient includes a hot wall correction and a blowing correction. The hot wall correction is given by Cohen and Reshotko:[27]

$$\Omega_{hw} = \left(\frac{\rho_{hw} \mu_{hw}}{\rho_{cw} \mu_{cw}} \right)^{0.1}. \tag{21}$$

The blowing correction is based on an empirical study by Kays and Crawford:[28]

$$\Omega_{blw} = \frac{\Phi}{e^\Phi - 1}, \tag{22}$$

where

$$\Phi = 2\lambda \frac{\dot{m}''}{\rho_e u_e C_{h_0}}. \tag{23}$$

The overall correction factor is the product of the two:

$$\left(\frac{C_h}{C_{h_0}} \right) = \Omega_{hw} \Omega_{blw}. \tag{24}$$

IV.   Numerical Solution Procedures

KATS discretized the governing equation (Eq. (11)) using first order backward Euler time integration and 2nd order spatial discretization. On each time step, the following discretized equation is solved for each control volume:

$$\left[\frac{V}{\Delta t} \frac{\partial \mathbf{Q}}{\partial \mathbf{P}} - \frac{\partial \mathbf{RHS}}{\partial \mathbf{P}} \right] \Delta \mathbf{P} = \mathbf{RHS}, \tag{25}$$

where $\mathbf{P}$, $\mathbf{Q}$, and $\mathbf{S}$ are vectors of primitive variables, conservative variables, and source terms, respectively, and the right hand side of the linear system is:

$$\mathbf{RHS} \equiv - \sum_{\text{faces}} (\mathbf{F} - \mathbf{F}_d) \cdot \mathbf{n} A + \mathbf{S} V \tag{26}$$

where $\mathbf{F}$ and $\mathbf{F}_d$ are respectively the matrices of convective and diffusive flux. The numerical scheme used to calculate the convective flux is AUSM+-up (Advection Upstream Splitting Method).[29] The first Jacobian matrix $\partial \mathbf{Q}/\partial \mathbf{P}$ in Eq. (25) is calculated analytically and the second Jacobian $\partial \mathbf{RHS}/\partial \mathbf{P}$ is obtained numerically via forward difference, where the perturbation to $\mathbf{P}$ is as small as the smallest positive floating-point number in double precision. KATS is paralleled using ParMETIS[30] for domain decomposition. On each domain, the linear system represented by Eq. (25) is solved via PETSc library,[31] where variables are passed through the interface using MPI.

V.   Test Cases

In this work, a slightly modified geometry is chosen as the computational domain, as depicted in Fig. 4. This is because numerical divergences were experienced when the extra hook-shaped geometry at the lower corner was considered. Although the modified mesh appears to be 2D, it is obtained by rotating the mesh along z-axis for 2 degrees and solved in 3D Cartesian coordinates.
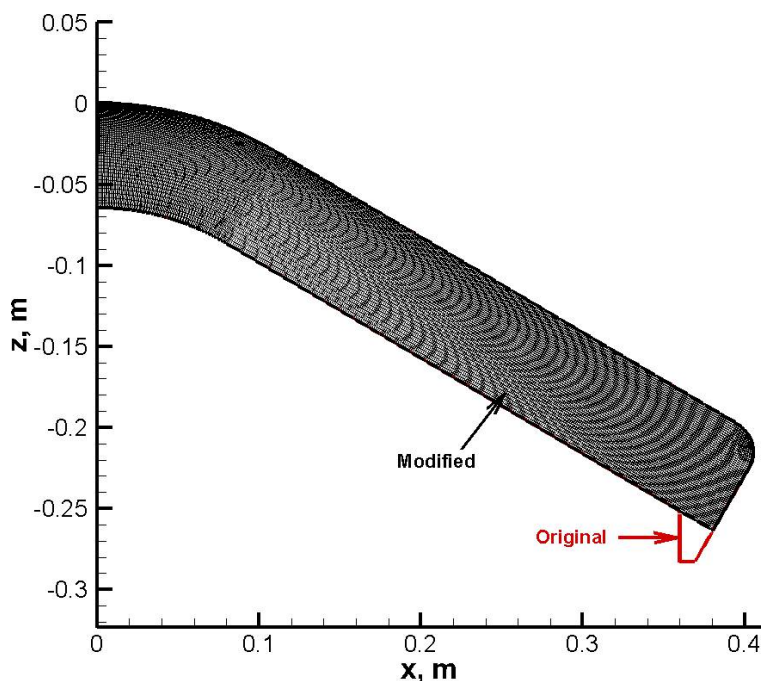

Figure 4: Original and modified heat shield geometry

The Stardust SRC Earth entry follows the trajectory given in Fig. 5. Boyd et. al. analyzed the 34 s and
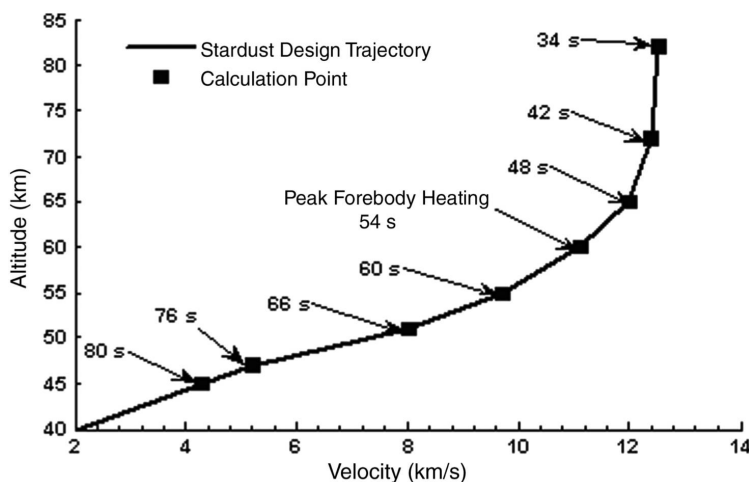

Figure 5: Stardust SRC reentry trajectory[2]

42 s trajectory points using both CFD and DSMC methods.[16] Before the mission, Olynick et. al. predicted the heat flux and pressure distribution on all seven trajectory points.[15] Using the surface heat flux and the surface pressure profiles presented in these two works, the entire heat shield response is simulated in this paper. The results of each case are presented in the following.

V.A. Heat shield response using surface boundary conditions provided in Boyd et. al.[16]

In Boyd et. al.,[16] two trajectories were considered: the 34 s (81 km) trajectory and the 42 s (71 km) trajectory. The surface heat flux and pressure distributions are shown in Fig. 6. Note that in Fig. 6a, the
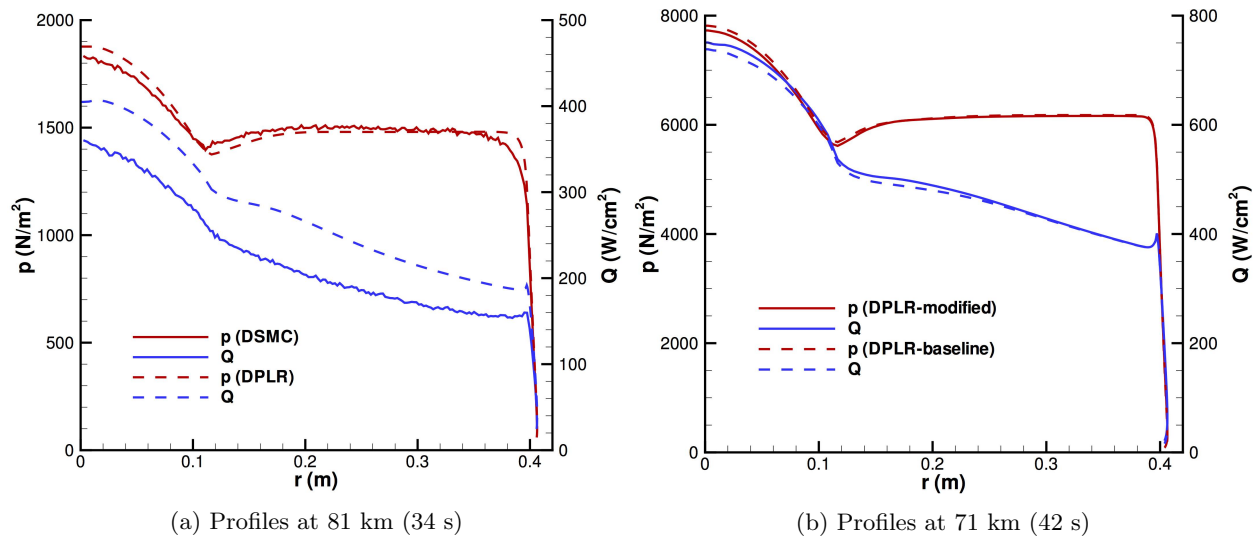

(a) Profiles at 81 km (34 s)　　　　　　　　(b) Profiles at 71 km (42 s)

Figure 6: Surface heat flux and pressure profiles given in Boyd et. al.[16]

CFD DPLR and DSMC results are quite different, which was claimed to be due to the near-continuum effects. In this work, the CFD DPLR results in Fig. 6a are selected, since the CFD profiles are continuous. For the 71 km (42 s) trajectory point, the DPLR-modified curves are chosen from Fig. 6b.

The simulation starts from 8 seconds before the first trajectory point to allow a smooth ramping, that is $t = 26$ s. The initial surface heat flux is assumed to be zero and the initial surface pressure is assumed to be the same as the minimum values in 34 s pressure profile. From $t = 26$ s to $t = 34$ s, the boundary conditions are linearly ramped from the initial values to the 34 s profiles given in Fig. 6a. After $t = 34$ s, the boundary conditions are linearly ramped from the 34 s profiles to the 42 s profiles. The boundary conditions stay at 42 s profiles for another 8 seconds after $t = 42$ s.

Since the original paper[16] was not designed to suit for material response simulation of an entire heat shield, the components of the surface heat flux was not mentioned. Therefore, the heat flux profiles provided in Fig. 6 are used to solve for the heat transfer coefficient first; then the correction factor is calculated and multiplied to the original surface heat flux. The radiation heating to the material is assumed to be taken into account by the applied heat flux profiles. The rest of the terms in the surface energy balance equation are modeled as discussed.

The initial conditions of the heat shield ablator is set to be the same as the environmental temperature and the initial gas pressure is set to be at 0.01 atm. Using these conditions, two 3D simulations are performed on the modified mesh given in Fig. 4, one with isotropic and the other with orthotropic materials. In addition, a 1D simulation is performed using the same conditions at the stagnation point. The 1D simulation setup is adopted from Weng and Martin.[10] The thickness of the 1D geometry is taken to be the same as the Stardust heat shield thickness, $i.e.$ 0.0645 m. Six thermocouples are selected along the centerline, and four are selected 0.008 m beneath the heat shield side wall. The coordinates of these thermocouples are given in Table 1. The locations of these thermocouples are illustrated in Fig. 7.

The temperature profiles at each thermocouple location are displayed in Fig. 8. Note that the values of temperature predicted in this work might be slightly higher than the exact value, since the (endothermic) ablation effect of the heat shield was not modeled. Unlike the situation seen for small test samples,[10] Fig. 8a shows that the surface temperatures are quite close between 1D, 3D isotropic, and 3D orthotropic models. For thermocouples 2, 3, and 4, the two 3D models all predicted higher temperatures than in the 1D model; and the temperatures were higher with the orthotropic model than with the isotropic model. The difference in temperatures is as high as 200 K between the orthotropic model and the 1D model. Note that, this behavior was also seen in small arc-jet test samples, where the extra heating was due to side wall heating and pyrolysis gas transport.[32] For the heat shield geometry considered in this study, the side wall heating

Table 1: Coordinates of thermocouples

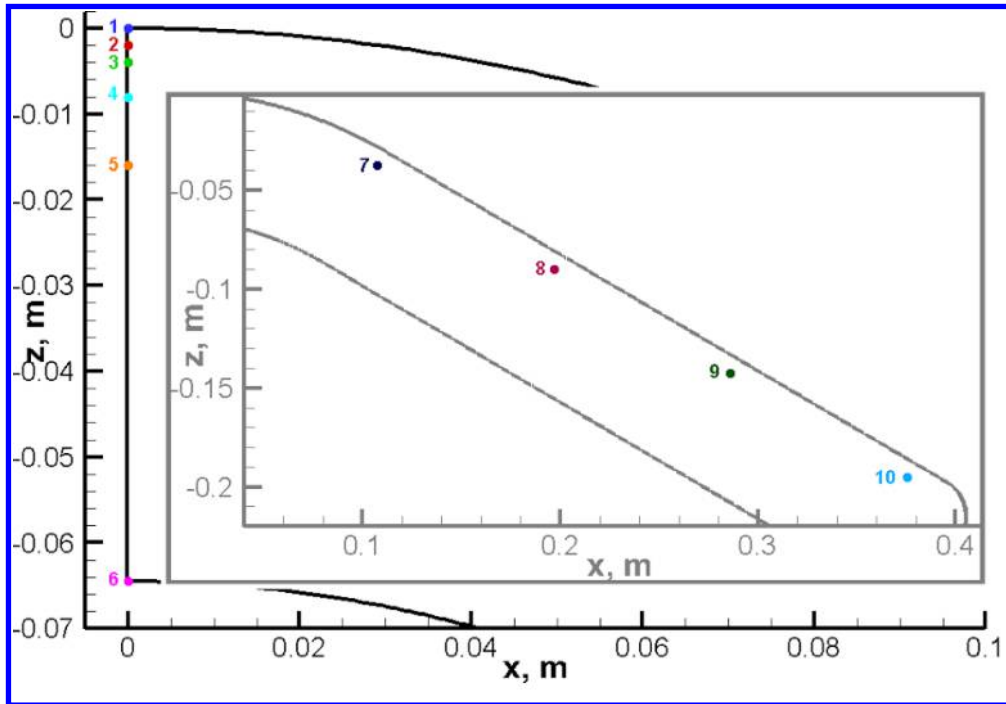| TC#	Coordinate (m)	TC#	Coordinate (m)
1	(0,0,0)	6	(0,0,-0.0645)
2	(0,0,-0.002)	7	(0.1077, 0, -0.0374)
3	(0,0,-0.004)	8	(0.1969,0,-0.0899)
4	(0,0,-0.008)	9	(0.2861,0,-0.1425)
5	(0,0,-0.03)	10	(0.3753,0,-0.195)

Figure 7: Thermocouple locations

effect should be less significant, because the side is very far from the centerline. Moreover, since the nose radius is much larger than the charring depth ($0.2202 \gg 0.008$ m), the front surface can be considered to be flat; thus the stagnation surface heating is very similar to a 1D heating. The discrepancies in temperature were more likely due to the pyrolysis gas transport. The theory behind gas transport heating the material is: gas generated in the decomposition zone of a charring ablator carries a great amount of enthalpy, which heats up the material as the gas travels within. The 1D model assumed the gas can only flow outside through the front, but the 3D models showed that the gas can flow literally inside, as shown in Fig. 9, which raised the centerline temperatures. Here, $|\dot{m}''| = \phi \rho_g \sqrt{(u^2 + v^2 + w^2)}$, which can be considered as an indication of local momentum of the pyrolysis gas. The streamlines in both Fig. 9a and 9b separate near the exposing surface, either blowing out or flowing inside and existing through the shoulder. Note that this behavior is quite similar to the one with iso-Q samples.[32] Finally, the orthotropic model had a higher permeability in the IP direction (parallel to the heat shield surface curvature) than the isotropic model, which encouraged more gas to travel within the material, and thus resulted in a higher centerline temperature.

Temperatures at thermocouples 5 ($z = -0.03$ m) and 6 (bond line) are constant, as shown in Fig. 8a, which suggests these two locations were not heated for the entire period of simulation. This suggests a very large safe factor was employed for the Stardust SRC heat shield, which is necessary for a planetary entry mission.

Figure. 8b presents the temperature histories at thermocouples 7 to 10. These thermocouples were located 0.08 m beneath the heat shield side wall. In contrast to the centerline results, the temperatures at these thermocouples were all lower with the orthotropic model than with the isotropic model. This is probably because the flow directions were almost paralleled to the heat shield surface, that the TTT component of
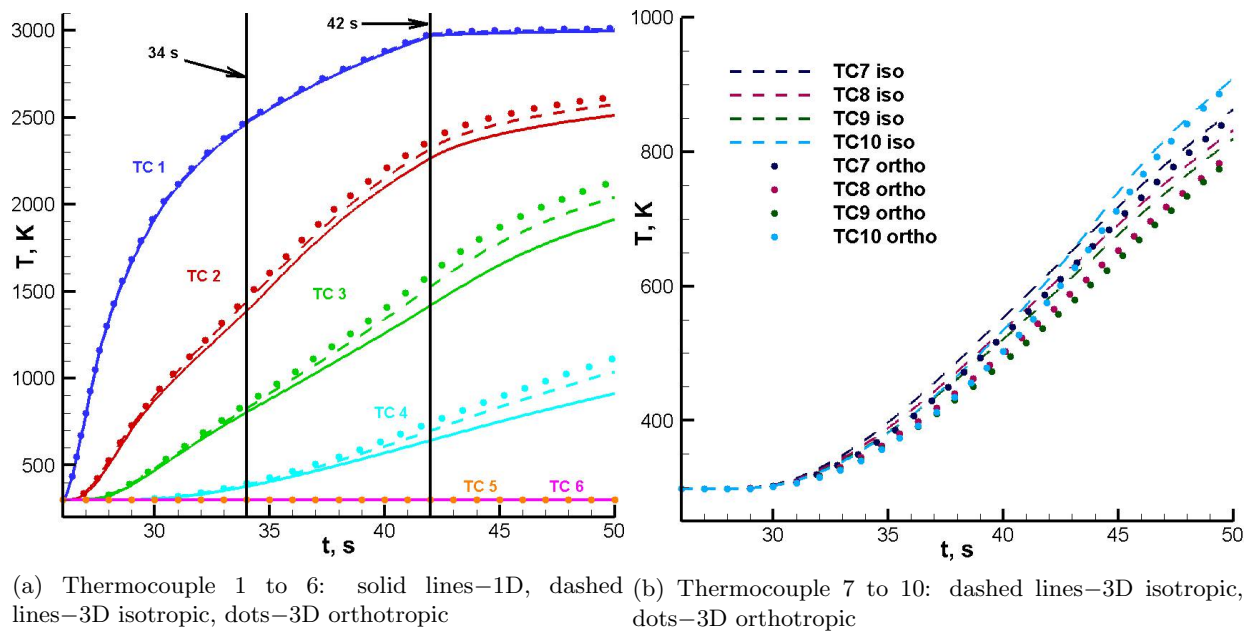
American Institute of Aeronautics and Astronautics Paper AIAA-2015-0211

(a) Thermocouple 1 to 6: solid lines−1D, dashed lines−3D isotropic, dots−3D orthotropic

(b) Thermocouple 7 to 10: dashed lines−3D isotropic, dots−3D orthotropic

Figure 8: Temperature histories at all thermocouple locations using Boyd's profiles
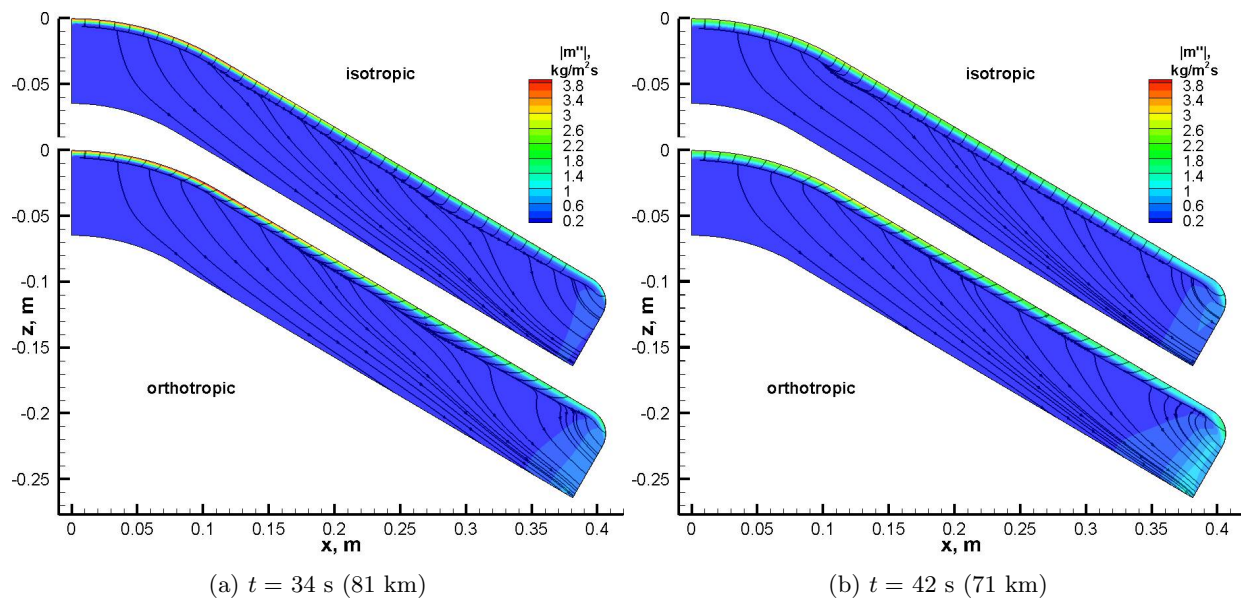

(a) $t = 34$ s (81 km)

(b) $t = 42$ s (71 km)

Figure 9: Pyrolysis gas momentum contours and streamlines using Boyd's trajectory profiles

gas transport (pointing vertically inside) was not as great as near the centerline; and the gas transport effect at these locations were dominated by the IP component, which carried the heat to the shoulder and out. As a result, the temperature at thermocouple 10 is even higher than at thermocouples 7 to 9.

The stagnation surface gas blowing rates are presented in Fig. fig: boyd blowing for all three models. It can be seen from the figure that the blowing rates for all three models were quite close for $26 < t < 29$ s; after $t = 29$ s, the three curves started to diverge, but the differences were not as great as for iso-Q samples.[10] The 1D model predicted the most surface blowing rate, which was expected since the front stagnation surface was the only exit for the gas in the 1D model. Pyrolysis gas modeled in 3D was able to travel inside, and therefore less gas was blown through the front. The orthotropic model had the least surface blowing rate, since it enabled more inward gas transport than the isotropic model.
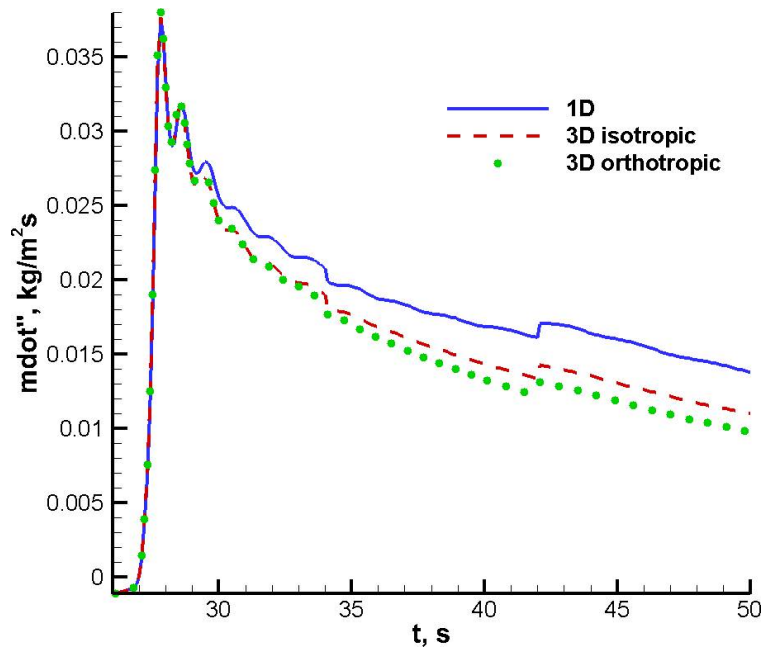
American Institute of Aeronautics and Astronautics Paper AIAA-2015-0211

Figure 10: Stagnation blowing rate using Boyd's trajectory profiles

V.B.   Heat shield response using surface boundary conditions provided in Olynick et. al.[15]

In order to investigate further along the trajectory, the surface heat flux and pressure distributions are extracted from Olynick et. al.[15] Olynick et. al. performed CFD calculations on seven trajectory points of the Stardust SRC Earth entry[15] . The total surface heat flux (without ablation assumption) and the pressure profiles are presented in Fig. 11 for all seven points.

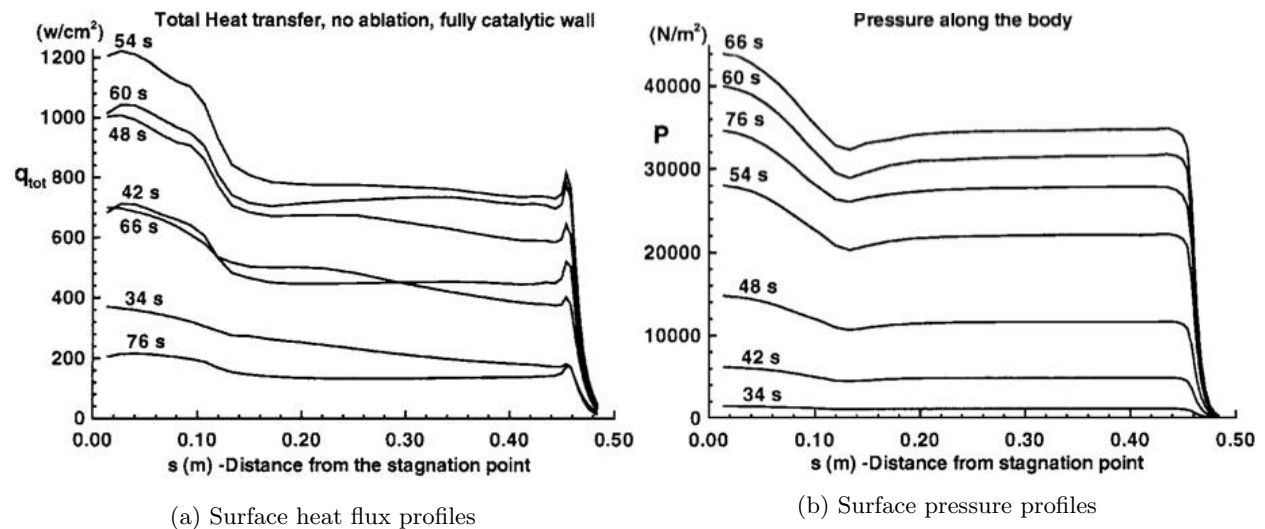(a) Surface heat flux profiles

(b) Surface pressure profiles

Figure 11: Stardust SRC forebody surface heat flux and pressure distribution for non-ablating surface[15]

In this case, the simulation also started from $t = 26$ s, *i.e.* 8 seconds before the 81 km trajectory. The setups for initial surface heat flux and initial surface pressure are identical to the previous study. The boundary conditions ramping between trajectories are also linear. The initial conditions and the computational mesh are identical to the previous simulation, *i.e.* $T_0 = T_\infty$, $p_0 = 0.01$atm, and the mesh is given in Fig. 4. The thermocouple locations are as same as in previous study, given in Table 1 and Fig. 7.

The temperature histories at various thermocouple locations are presented in Fig. 12. For the first six thermocouples along the centerline, as shown in Fig. 12a, surface temperature didn't vary much between
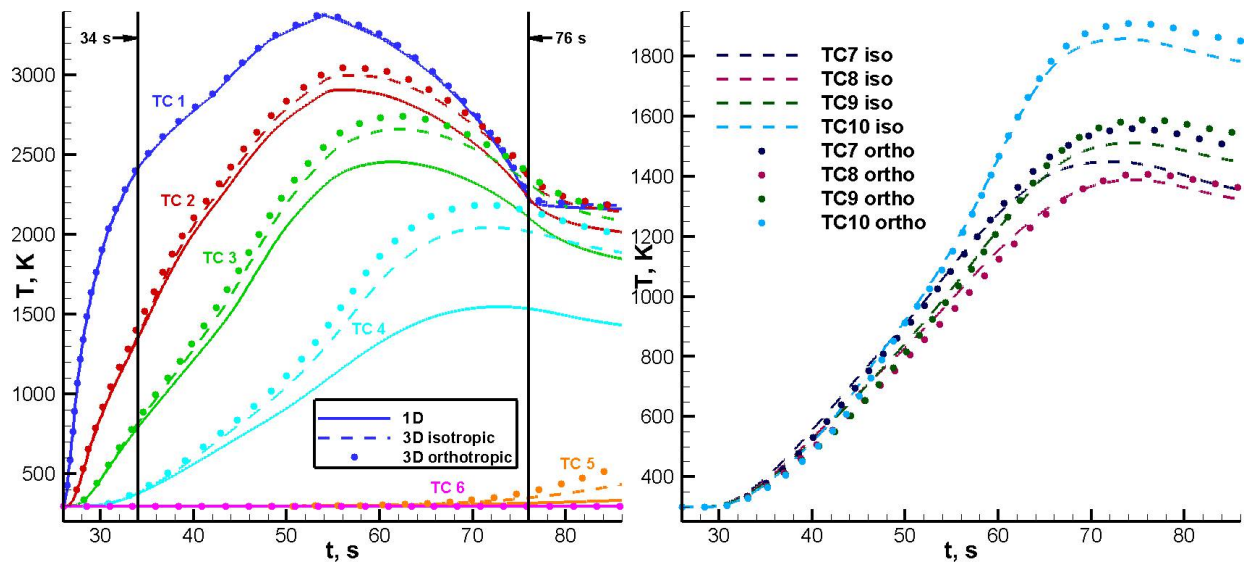
American Institute of Aeronautics and Astronautics Paper AIAA-2015-0211

(a) Thermocouple 1 to 6: solid lines−1D, dashed lines−3D isotropic, dots−3D orthotropic

(b) Thermocouple 7 to 10: dashed lines−3D isotropic, dots−3D orthotropic

Figure 12: Temperature histories at all thermocouple locations using Olynick's profiles

models; for thermocouple 2 to 5, the 3D orthotropic model predicted the highest temperature, followed by the 3D isotropic model, and the 1D model predicted the least temperature; the bond line temperature for all models didn't change. The analysis for these thermocouples would be the same as for the Boyd's profiles. It is worth to mention that, in this case, the difference in temperature between the orthotropic and 1D model was as high as about 700 K, at TC 4, $t = 70$ s. In addition, the 3D models picked up temperature rises at TC 5, which was not seen in the 1D model. These captured differences were quite significant, and impropriate modeling may lead to failure of the heat shield or overheating of the payloads in the substructure.

For the second set of thermocouples shown in Fig. 12b, the temperatures of the orthotropic model were initially lower than the ones of the isotropic model; but they eventually exceeded the latter. This behavior was not seen in the previous study using Boyd's profiles, where the simulation time was short. In this case, the simulation time was long enough to allow the decomposition zone to reach beyond these thermocouple locations. When the materials at these locations were charred, the pyrolysis gas transports towards these locations are from the high-temperature decomposition zone. With the enhanced gas transport (higher permeability), the orthotropic model would predict a higher temperatures than the isotropic model.

VI.   Concluding Remarks

As a conclusion, the Stardust SRC Earth entry surface boundary conditions were extracted from two aerodynamics papers.[16,15] These boundary conditions are applied to the whole heat shield geometry to perform material response simulations using KATS with the newly developed permeability model. The objective is to investigate whether the 1D model is representative to the 3D material response of the entire heat shield. Based on this study, the surface temperature of the 1D model were not very far from the 3D models, but the centerline temperatures within the material were very different; the difference can be as significant as 700 K. This was due to the fact that, the pyrolysis gas generated within the decomposition zone has a great enthalpy, which can heat up the material significantly, especially considering the heating condition for an atmospheric entry is quite severe. The temperature of the material at the heat shield shoulder was higher than along the side, since the hot gas traveling inside were expelled through the shoulder. The orthotropic model also showed a significant difference to the isotropic model.

On the numerical aspect, the authors experienced great obstacles initially in performing simulations over the heat shield geometry. The initial conditions of the heat shield were tricky to set. Physically, the heat shield should stay at the environmental conditions before the reentry. However, the environmental pressure is usually much less than the atmosphere pressure, and this may lead to divergent solution with

the existing numerical model, since the pressure gradients at the surface will be dominant. This instability can be bypassed by reducing time step. Based on the experience from this work, the time step size required three to four order of magnitude smaller than the values normally assigned for small test samples, in order to prevent divergence of the solution. This requirement leads to huge computational run time. In addition, the temperature solution with the environmental initial conditions eventually converges to 298 K, which is the reference temperature of the TACOT material. When initial temperature was set to the reference temperature, the computation time was greatly saved by allowing a much larger time step without divergence. This suggests that extra material models might be needed for ablators at low temperature.

In summary, 1D models is a relatively good assumption to the stagnation temperature, but might not be accurate for the in-depth material response. The shoulder region response also might be very different from the 1D assumptions. Additional models might be needed for charring ablators at low temperature. Orthotropic properties model is necessary for an accurate heat shield material response analysis and design.

VII.   Acknowledgments

References

[1]Bose, D., Olson, M., Laub, B., White, T., Feldman, J., Santos, J., Mahzari, M., MacLean, M., Dufrene, A., and Holden, M., "Initial Assessment of Mars Science Laboratory Heatshield Instrumentation and Flight Data," in "51st AIAA Aerospace Sciences Meeting," AIAA Paper 2013-908, Grapevine, TX, 2013, doi:10.2514/6.2013-908.

[2]Beerman, A. F., Lewis, M. J., Starkey, R. P., and Cybyk, B. Z., "Significance of Nonequilibrium Surface Interactions in Stardust Return Capsule Ablation Modeling," *Journal of Thermophysics and Heat Transfer*, Vol. 23, No. 3, 2009, p. 425, doi:10.2514/1.38863.

[3]Mansour, N. N., Panerai, F., Martin, A., Parkinson, D. Y., MacDowell, A. A., Haboub, A., Sandstrom, T. A., Fast, T., Vignoles, G. L., and Lachaud, J., "A New Approach To Light-Weight Ablators Analysis: From Micro-Tomography Measurements to Statistical Analysis and Modeling," in "44th AIAA Thermophysics Conference," AIAA, San Diego, CA, 2013, doi:10.2514/6.2013-2768.

[4]Moyer, C. B. and Rindal, R. A., "AN ANALYSIS OF THE COUPLED CHEMICALLY REACTING BOUNDARY LAYER AND CHARRING ABLATOR PART II," Contractor Report CR-1060, NASA, 1968.

[5]Chen, Y.-K. and Milos, F. S., "Ablation and Thermal Response Program for Spacecraft Heatshield Analysis," *Journal of Spacecraft and Rockets*, Vol. 36, No. 3, 1999, pp. 475–483, doi:10.2514/2.3469.

[6]Martin, A. and Boyd, I. D., "Non-Darcian Behavior of Pyrolysis Gas in a Thermal Protection System," *Journal of Thermophysics and Heat Transfer*, Vol. 24, No. 1, 2010, pp. 60–68, doi:10.2514/1.44103.

[7]Amar, A. J., Blackwell, B. F., and Edwards, J. R., "One-Dimensional Ablation Using a Full Newton's Method and Finite Control Volume Procedure," *Journal of Thermophysics and Heat Transfer*, Vol. 22, No. 1, 2008, pp. 71–82, doi:10.2514/1.29610.

[8]Blackwell, B. F. and Hogan, R. E., "One-Dimensional Ablation Using Landau Transformation and Finite Control Volume Procedure," *Journal of Thermophysics and Heat Transfer*, Vol. 8, No. 2, 1994, pp. 282–287, doi:10.2514/3.535.

[9]Ahn, H.-K., Park, C., and Sawada, K., "Response of Heatshield Material at Stagnation Point of Pioneer-Venus Probes," *Journal of Thermophysics and Heat Transfer*, Vol. 16, No. 3, doi:10.2514/2.6697.

[10]Weng, H. and Martin, A., "Multidimensional Modeling of Pyrolysis Gas Transport Inside Charring Ablative Materials," *Journal of Thermophysics and Heat Transfer*, Vol. 28, No. 4, 2014, pp. 583–597, doi:10.2514/1.T4434.

[11]Chen, Y.-K. and Milos, F. S., "Two-Dimensional Implicit Thermal Response and Ablation Program for Charring Materials," *Journal of Spacecraft and Rockets*, Vol. 38, No. 4, 2001, pp. 473–481, doi:10.2514/2.3724.

[12]Chen, Y.-K. and Milos, F. S., "Three-Dimensional Ablation and Thermal Response Simulation System," in "38th Thermophysics Conference," Toronto, Ontario Canada, AIAA 2005-5064, 2005, doi:10.2514/6.2005-5064.

[13]Lachaud, J. and Mansour, N. N., "A pyrolysis and ablation toolbox based on OpenFOAM - with application to material response under high-enthalpy environments," in "5th OpenFOAM Workshop," Chalmers University, Gothenburg, Sweden, 2010.

[14] Amar, A. J., Calvert, N. D., and Kirk, B. S., "Development and Verification of the Charring Ablating Thermal Protection Implicit System Solver," in "49th AIAA Aerospace Sciences Meeting and Exhibit," Orlando, FL, AIAA paper 2011-144, 2011, doi:10.2514/6.2011-144.

[15] Olynick, D., Chen, Y.-K., and Tauber, M. E., "Aerothermodynamics of the Stardust Sample Return Capsule," *Journal of Spacecraft and Rockets*, Vol. 36, No. 3, 1999, pp. 442–462, doi:10.2514/2.3466.

[16] Boyd, I. D., Trumble, K., and Wright, M. J., "Nonequilibrium Particle and Continuum Analyses of Stardust Entry for Near–Continuum Conditions," in "39th AIAA Thermophysics Conference," Miami, FL, AIAA Paper 2007-4543, 2007, doi:10.2514/6.2007-4543.

[17] Trumble, K. A., Cozmuta, I., Sepka, S., Jenniskens, P., and Winter, M., "Postflight Aerothermal Analysis of the Stardust Sample Return Capsule," *Journal of Spacecraft and Rockets*, Vol. 47, No. 5, 2010, pp. 765–774, doi:10.2514/1.41514.

[18] "http://www.nasa.gov/mission_pages/stardust/multimedia/capsule-1.html," .

[19] Tran, H. K., Johnson, C. E., Rasky, D. J., Hui, F. C. L., Hsu, M.-T., Chen, T., Chen, Y. K., Paragas, D., and Kobayashi, L., "Phenolic impregnated carbon ablators (PICA) as thermal protection systems for discovery missions," Technical Report 110440, NASA Technical Memorandum, 1997.

[20] Johnson, C. E., Tran, H. K., Smith, M., Dill, H., and Etienne, L., "Stardust Backshell and Back Interface Plate Design Verification Tests in the NASA Ames Arc Jet Facilities," AIAA Paper 1997-2483, 1997, doi:10.2514/6.1997-2483.

[21] Lachaud, J., Martin, A., Cozmuta, I., and Laub, B., "Ablation test-case series #1," in "4th AFOSR/SNL/NASA Ablation Workshop," Albuquerque, NM, 2010.

[22] Marschall, J. and Milos, F. S., "Gas permeability of rigid fibrous refractory insulations," *Journal of Thermophysics and Heat Transfer*, Vol. 12, No. 4, 1998, pp. 528–535, doi:10.2514/2.6451.

[23] Marschall, J. and Cox, M. E., "Gas Permeability of Lightweight Ceramic Ablators," *Journal of Thermophysics and Heat Transfer*, Vol. 13, No. 3, 1999, pp. 383–386, doi:10.2514/2.6451.

[24] Stackpoole, M., Sepka, S., Cozmuta, I., and Kontinos, D., "Post-Flight Evaluation of Stardust Sample Return Capsule Forebody Heatshield Material," in "46th AIAA Aerospace Sciences Meeting and Exhibit," Reno, Nevada, AIAA 2008-1202, 2008, doi:10.2514/6.2008-1202.

[25] Martin, A. and Boyd, I. D., "Simulation of pyrolysis gas within a thermal protection system," in "40th Thermophysics Conference," Seattle, WA, AIAA Paper 2008-3805, 2008, doi:10.2514/6.2008-3805.

[26] Gosse, R., "Pyrolysis Gas Modeling of TPS Material Using Finite-Volume Method and Issues with Validation," in "42nd AIAA Thermophysics Conference," AIAA 2011-3641, 2011, doi:10.2514/6.2011-3641.

[27] Cohen, C. B. and Reshotko, E., "Similar Solutions for the Compressible Laminar Boundary Layer with Heat Transfer and Pressure Gradient," Tech. Rep. 1293, NACA, 1955.

[28] Kays, W. M., Crawford, M. E., and Weigand, B., *Convective Heat and Mass Transfer*, McGraw-Hill, 4th ed., 2005.

[29] Liou, M.-S., "A sequel to AUSM, Part II: AUSM+-up for all speeds," *Journal of Computational Physics*, Vol. 214, No. 1, 2006, pp. 137 – 170, doi:10.1016/j.jcp.2005.09.020.

[30] Schloegel, K., Karypis, G., and Kumar, V., "Parallel Multilevel Algorithms for Multi-Constraint Graph Partitioning," in "Euro-Par," LNCS 1900, 2000, pp. 296–310, doi:10.1007/3-540-44520-X_39.

[31] Balay, S., Brown, J., Buschelman, K., Gropp, W.-D., Kaushik, D., Knepley, M.-G., McInnes, L.-C., Smith, B.-F., and Zhang, H., "PETSc Web page http://www.mcs.anl.gov/petsc," , 2013.

[32] Weng, H. and Martin, A., "Numerical investigation of pyrolysis gas blowing pattern and thermal response using orthotropic charring ablative material," *Journal of Thermophysics and Heat Transfer*, doi:10.2514/1.T4576. In Press (Control ID 2014-09-T4576).